Journal of The
Electrochemical Society

Deciphering the Impacts of Al, Fe, Li Sulfate Impurities on the Synthesis and Performances of $LiNi_{0.6}Mn_{0.2}Co_{0.2}O_2$ Cathode Materials

To cite this article: Johann Chable *et al* 2025 *J. Electrochem. Soc.* **172** 020532

Journal of The Electrochemical Society, 2025 **172** 020532

Deciphering the Impacts of Al, Fe, Li Sulfate Impurities on the Synthesis and Performances of $LiNi_{0.6}Mn_{0.2}Co_{0.2}O_2$ Cathode Materials

Johann Chable,[z] Nicole Bohn, Monika Raab, Shadi Al-Tobul, Thomas Bergfeldt, Marcus Müller, and Joachim R. Binder

Institute for Applied Materials, Energy Storage Systems, Karlsruhe Institute of Technology, Hermann-von-Helmholtz-Platz 1, 76344, Eggenstein-Leopoldshafen, Germany

The recycling of $LiNi_{0.6}Mn_{0.2}Co_{0.2}O_2$ cathode active material (CAM) from Li-ion batteries cannot avoid the presence of impurities in the recycled Ni-, Co-, or Mn sulfates. The precise understanding of the impurities influence on the resynthesis is of uttermost importance. To tackle this goal, this study simulated the resynthesis process by adding on purpose and separately Al-, Fe-, and Li-sulfate in the regular CAM synthesis. Their effects on the morphology, elemental composition, crystal structure, and electrochemical performances of $Ni_{0.6}Mn_{0.2}Co_{0.2}M_x(OH)_2$ and $LiNi_{0.6}Mn_{0.2}Co_{0.2}M_xO_2$ were systematically investigated for x = 0.0005, 0.005, and 0.05. The in-house reference material synthesized via a coprecipitation reaction allowed to produce a well-characterized basis. Above $x_{Al} = 0.0005$, the hydroxide secondary particles lost their spherical form and above $x_{Fe} = 0.005$, the crystal structure was affected. Both effects led to cell capacity decay, contrary to the discrete influence of Li. The absence of any positive effects reported by similar studies, the complexity of the various influences of these foreign ions and the limitations of the coin cells tests were pointed out. These results are a solid groundwork for future academic and industrial studies in the field of circular economy, by determining a tolerance threshold for each impurity.

 [DOI: 10.1149/1945-7111/adb64e]

Manuscript submitted December 19, 2024; revised manuscript received January 31, 2025. Published February 26, 2025.

Supplementary material for this article is available online

Glossary

TM	Transition Metal
XRD	X-ray diffraction
AM	Active Material
CAM	Cathode Active Material
pCAM	Precursor of Cathode Active Material
STR	stirred tank reactor
NMC 111	$LiNi_{0.33}Mn_{0.33}Co_{0.33}O_2$
NMC 622	$LiNi_{0.6}Mn_{0.2}Co_{0.2}O_2$
EDX	Energy-Dispersive X-ray spectroscopy
NCA	$LiNi_xCo_yAl_zO_2$
LDH	Layered Double Hydroxide phase

Among the various batteries-related themes, recycling is still quite emerging but is gaining attention in the scientific community, due to its importance regarding environmental,[1] economic[2] and geopolitical concerns.[3] Even if some processes already reached industrial relevance,[4,5] recycling remains an interesting topic for fundamental and applied research, dealing with non-trivial and cross-disciplinary questions,[6] like the precise separation and efficient recovery of the different battery elements and the deeper understanding of the morphology-crystal structure-electrochemical performances relationships.[7,8] In the case of Li-ion batteries, the most-explored recycling technologies are pyrometallurgy, hydrometallurgy and direct recycling.[9] Pyrometallurgy is principally based on shredding and sorting the battery cells to recover the so-called black mass, which is then pyrolyzed to recover metal ingots, while hydrometallurgy uses water-based chemistry to separate the different elements constituting the black mass.[10] Direct recycling intends to favorize the reuse of the cathode active materials without having to destroy the cells or to come back to the starting chemicals but still is rather confined to laboratory scale at the moment.[11]

Given the high energetic cost of pyrometallurgy, hydrometallurgy currently has the upper hand in the choice for a recycling method.[9] It can generate high yields for the recovery of critical elements like Ni, Mn and Co,[12] but involves the use of corrosive chemicals (e.g. concentrated sulfuric acid for the leaching), of organic additives and of multiple separation steps, depending on the pH-value.[13] Each part of this process can be the source of the presence of foreign ions in the recycled material, which may have some detrimental effects on the performances of the new batteries based on it, as summed-up recently by Kim et al.[14] Determining the amount and the impact of each possible impurity is therefore of greatest importance for the improvement of the hydrometallurgical process towards large scale industrialization. There have been a lot of studies dealing with the influence of different elements on diverse NMC concentrations (NMC = $LiNi_xMn_yCo_zO_2$ with x+y+z = 1, generally labelled NMC 111, 622 or 811 to recall the xyz values). Nevertheless, most of it was more related to doping or planned substitution,[15–18] focused on the oxide and its crystal structure without much regards to the hydroxide, introduced the impurity only during the mixing and calcination step or used quite high impurity concentrations (above 1 at%)[19,20] that should rarely be encountered in concrete recycling applications.[21,22]

To the best of our knowledge, only few articles directly tackled the simplest question, i.e. introducing an impurity at the start of the normal synthesis of the precursor of the cathode active material (pCAM) without changing any parameter and characterizing the outcome. This was the case of the Kwon group and of the Wang group, for example with Al in NMC 111[23] or 622,[24] Fe in NMC 111[25] or 622[26] and Li in NMC 111.[27] Aluminium was found to have a noticeable impact on the secondary particle formation and size at high amounts, which led to decreased electrochemical performances, such as lower initial discharge capacity, capacity retention or coulombic efficiency. Small amounts could have positive effects,[24] but these were at best limited and should be confirmed by further studies. This positive-negative effects dichotomy seemed to exist in the case of iron as impurity,[25] too, but quite dependent on its valence in the used precursor.[26] The concrete source of these changes remained to be understood, some works bringing the hypothesis of structural modifications, like a reduced Li/Ni disorder, especially for NMC 811.[28] A possible disturbance of Li seemed counterintuitive as its presence is expected in the final CAM but it is normally brought only after the hydroxide synthesis. As was shown in the work of Jo

[z]E-mail: johann.chable2@kit.edu

et al.[27] residual Li (most probably in the form of Li_2SO_4) left the hydroxide morphology untouched but altered the crystallinity of both pCAM and CAM, at least when the hydroxide was not washed after coprecipitation.

To prolong and refine these findings, this study proposes to plunge to even lower concentration domains in order to identify the threshold of the impurity influence on the synthesis of NMC 622. This should allow to propose practical limits for three foreign ions not to overcross to avoid any undesirable effects in a future resynthesis process, which should provide interesting insights to both industry and fundamental research. It would also be a good basis to later disentangle the effects of various impurities, whether they would be purposely mixed or randomly present in a recycled material, along with organics or anions. The focus of this study was thus put at first on the precise characterization of $Ni_{0.6}Mn_{0.2}Co_{0.2}(OH)_2$ and of $LiNi_{0.6}Mn_{0.2}Co_{0.2}O_2$ reference materials, obtained with an ordinary coprecipitation synthesis technique. These standards reached practical goals: being as pure as possible, with an easy-to-scale synthesis method, with forms and dimensions close to real applications (spherical particles with a d_{50} diameter of about 10 μm) and with an acceptable discharge capacity (defined as at least 150 mAh g^{-1} at 1 C). In a second time, the presence of impurities was simulated by introducing low amounts of aluminium-, iron- and lithium sulfate, respectively, and by following the exact same synthesis and characterization procedures as for the reference materials. Their impacts were found at different steps of the CAM production, on the hydroxide morphology and crystal structure for aluminium and lithium whereas rather on the oxide crystal structure for iron. Threshold concentrations for each of these three elements were identified and discussed, regarding the magnitude of the electrochemical perturbations that resulted of the materials modification.

Experimental

Materials and methods.— *Standard solutions.*—The following commercial transition metal (TM) sulfates were obtained from VWR Chemicals ($NiSO_4.6H_2O$, 100% and $MnSO_4.H_2O$, 100%) and Alfa Aesar ($CoSO_4.7H_2O$, ⩾98%). All commercially purchased precursors were used as received, without further purification. From these, a mixed sulfate solution was prepared by dissolving and combining the respective TM salts in deionized water in a molar ratio of M = Ni/Co/Mn = 6/2/2 to achieve an overall metal concentration of 2 mol l^{-1}.

A sodium hydroxide solution (10 mol l^{-1}) was prepared by dissolving commercially purchased NaOH pellets (Merck KGaA, pellets for analysis) in deionized water, as well as two ammonia solution (5 M and 1 M) and a hydrochloric acid solution (1:10) by diluting commercial solutions (Honeywell Fluka, 30–33% NH_3 and Thermoscientific, HCl 37%, respectively) in deionized water.

Each solution was always prepared new and fresh maximum 3 days before use, stored in closed bottles and agitated again for ≈15 min prior to use on the synthesis day.

Impurities-containing solutions.—Impurities-containing solutions were prepared by adding $Al_2(SO_4)_3.18H_2O$ (Carl Roth, reinst.), $FeSO_4.7H_2O$ (VWR Chem, 99.5%) or $Li_2SO_4.H_2O$ (Thermoscientific, ⩾99.0%) to the TM sulfates solution, respectively. The 6/2/2 ratio and the 2 mol l^{-1} concentration were kept unchanged. These precursors were also used without any further purification.

Coprecipitation of $Ni_{0.6}Co_{0.2}Mn_{0.2}(OH)_2$.—$Ni_{0.6}Co_{0.2}Mn_{0.2}(OH)_2$ particles were prepared batch wise in a 2 l stirred-tank glass reactor, equipped with a LabManager® unit (HiTec Zang GmbH, Germany), allowing to monitor the solutions feeding rates, the temperature and the pH-value (a picture of the self-constructed reactor setup is available on Fig. S1). The reactor possessed a double-wall system, for deionized water to circulate in it and heat the reaction (Haake DC 30, Thermoscientific), a blade stirrer with a length of 10 cm, a Teflon-coated thermometer, a pH-probe (EX pH-E SL 80–360 PH, Xylem Analytics) and three dosing tubes (Tygon, 2 mm internal diameter, Ismatec) for the respective reactant solutions; the TM sulfate solution, the ammonia solution and the sodium hydroxide solution. The solutions were pumped into the reactor thanks to peristaltic pumps (ISM 597D Reglo Digital, Ismatec), and the tubes were positioned so as to avoid touching each other, as well as the inner rand of the reactor. LabVision® software (Hitec Zang GmbH) allowed to program the synthesis path (Fig. S2), to have control and live track of all of the relevant synthesis parameters.

Prior to each synthesis, the pumps were calibrated by comparing expected and obtained masses of each solution, the pH-probe was calibrated at room temperature by using buffer solutions with $pH_{20°C}$ = 7.0 and $pH_{20°C}$ = 10.0 (ROTI®STAR, Carl Roth), ≈ 350–400 ml of the 1 M NH_3 solution were introduced in the reactor; enough to have both the thermometer and the pH-probe immersed in the solution and a gentle nitrogen gas bubbling was started directly in the solution. The nitrogen flow was only stopped after the complete collection of the product.

Conducting the coprecipitation reaction meant mixing the TM sulfates solution droplet-wise at a rate of 30 g h^{-1} with the 5 M NH_3 solution at a rate of 15 g h^{-1}, while stirring the whole solution at 500 rpm and maintaining a temperature of 50 °C and a pH-value of 11 ± 0.02. After 5 h of reaction time, the sulfates and ammonia flows were stopped but the stirring was kept for further 18 h (Fig. S2).

The obtained product suspension was let to stir until being collected, centrifugated, washed and dried. The centrifugation was conducted at 3900 rpm for 5 min (Varifuge 20 RS, Heraeus) in two separate 500 ml Nalgene™ flasks (PPCO, Thermofischer). After each centrifugation step, the supernatant was disposed of and the solid part was washed by deionized water. After three centrifugation steps, the pH-value of the supernatant was already measured at 7. In the end, the last supernatant was removed and the solid product was dried in air at 80 °C for 17 h in an oven (OMS60, Heratherm). If necessary, the dried product was softly grinded in an agate mortar for 5 min to obtain a fine powder for further characterizations. The powder density ρ_{geo} was estimated roughly geometrically, based on the volume occupied in the collecting vial (V) and the following equation: $\rho_{geo} = \frac{m}{V}$, where m is the sample mass.

The reactor and the feeding tubes were cleaned three times after each synthesis to avoid any cross-contamination from the different impurities: once with the HCl-diluted solution and twice with deionized water, by stirring at 700 rpm.

Coprecipitation of $Ni_{0.6}Co_{0.2}Mn_{0.2}M_x(OH)_2$ with M = Al, Fe, Li.—The coprecipitation synthesis of the impurities-containing products was conducted with the exact same process as described here above, by only switching to another TM sulfate solution, containing the targeted impurity as dissolved sulfate.

Cathode active material synthesis.—The hydroxide compounds obtained from the coprecipitation synthesis were mixed by ball-milling with commercially obtained Li_2CO_3 (⩾99.0%, Merck KGaA) in an 80 ml ZrO_2 jar (Fritsch GmbH, Germany). 5 at %-excess of Li_2CO_3 were provided to take the possible Li-loss during the calcination into account. Ø 3 mm yittria-stabilized zirconia balls were used with a ball to powder mass ratio of 12, the whole being covered by 25 g of isopropanol. 5 steps of 10 min milling and 5 min break were conducted at 100 rpm in a Pulverisette 7 Premium line device (Fritsch GmbH, Germany). After milling, the balls were sieved out and the resulting powder dried in air at 80 °C for 17 h.

6 g of this mixture were then placed in an Al_2O_3 crucible to be calcined under synthetic air (2 l min^{-1} for 15 min then 1 l min^{-1}) in an oven (CWF1223, A105 Retort, Carbolite Gero Ltd., England). The calcination was conducted in two steps: a first dwell step at 550 °C for 3 h (reached in 2 h ≡ heating rate of ≈ 4.4 °C min^{-1}) was followed by a second dwell step at 900 °C for 10 h (reached in 1 h ≡ heating rate of ≈ 5.8 °C min^{-1}). The oven was let to cool down naturally until 30 °C, when the product was taken out and grinded in

an agate mortar for 5 min to obtain a powder for further characterizations.

Material characterization.— *Elemental analysis.*—Elemental analysis (EA) was conducted using inductively coupled plasma optical emission spectrometry (ICP-OES, iCAP 7600 DUO, Thermo Fisher Scientific) to determine the amount of the following elements: Li, B, Na, Al, Si, Ca, Mn, Fe, Co, Ni and Zr. About 100 mg of the samples (weighing accuracy ± 0.05 mg) were extracted in acid in a graphite oven (EasyDigest, Analab). The analysis of the elements was accomplished with four different calibration solutions and an internal standard (Sc). The range of the calibration solutions did not exceed a decade. The two or three major wavelengths of the elements has been used for calculation. Each material was sampled at least three times.

The carbon content was measured with a CS-analyser (CS 600, LECO) and nitrogen and oxygen contents with carrier gas hot extraction (TGHE, G8 GALILEO, Bruker AXS).

The stoichiometry was calculated back with the following assumption: $x_{Ni} + x_{Mn} + x_{Co} = 1$.

Laboratory powder X-ray diffraction measurements (PXRD).—PXRD patterns were collected ex situ at room temperature on a laboratory powder diffractometer (D2-Phaser, Bruker) with Cu $K\alpha_{1,2}$ radiation (mean wavelength $\lambda = 1.54056$ Å) in a Bragg-Brentano geometry with 30 kV and 3 mA and a Lynxeye XE-T detector. Each pattern was measured in a 2θ range from 6.0 to 80 2θ, applying a step size of 0.01 2θ and a step duration of 5 s (total scan time of ≈10 h). Sample holders were rotated during the measurements at 1 rpm. The program Fullprof[29] was used for Profile Matching refinements of the cell parameters of the materials with help of the Le Bail Method.[30]

SEM and EDX.—Imaging of the active material and coated electrodes was performed using a field-emission scanning electron microscope (Supra 55, Carl Zeiss GmbH, Oberkochen, Germany). Characteristic SEM images were taken by systematically choosing the same magnifications (×100, ×500, ×1000, ×5000, ×10000 and ×25000). The representativity of the images was verified on other places (at least two different areas per sample and per magnification). Cross-sections were prepared by ion-beam milling (EM TIC3X, Leica Microsystems GmbH, Wetzlar, Germany) using argon ions and an accelerating voltage of 6 kV at 2.2 mA gun current. Energy-dispersive X-ray spectroscopy (EDX) analysis was carried out with an Ultim Extreme silicon drift detector (Oxford Instruments, UK) with Aztec software at an acceleration voltage of 4 kV.

Particle size distribution.—Measurement of the secondary particle size distribution was performed using laser scattering based on the Mie scattering theory (Partica LA-960 V2, Horiba Scientific, Japan). Samples were prepared by dispersing a small amount of cathode powder in deionized H_2O with the help of ultrasonic agitation (Sonopuls HD4200, Bandelin Electronic GmbH, Germany) using a pulse of 0.5 s every 1.0 s during 30 s with 10% amplitude. The cathode particles were assumed to have a refractive index of 1.9–3.7 (Ni), and 1.33 was taken for deionized H_2O as dispersant. The intensity of the scattered laser beam was measured as a function of the scattering angle for particle sizes in the range of 0.05 μm to 5000 μm (a combination of red and blue light was utilized). Five measurements per sample were performed, and average values were calculated.

BET and porosimetry.—The specific surface area was determined through N_2 adsorption with evaluation by Brunauer–Emmett–Teller (BET) theory in the linear pressure range (Gemini VII 2390, Micromeritics Instruments Corporation, Norcross, GA, USA). Porosity of the particles was measured with Mercury intrusion (CEI Pascal 1.05, Pascal 140 EVO/Pascal 440 EVO, ThermoElectron S.p.A., Milan, Italy). The internal porosity P was calculated according to the equation: $P = \frac{V_p}{V_p + 1/\rho}$, where Vp is the inner specific pore volume, between 4 and 116 nm of pore size, and ρ the density (3.8 g cm^{-3} for the NMC 622 hydroxide and 4.5 g cm^{-3} for the oxide).

Electrochemical measurements.— *Electrodes preparation.*—The slurries used for electrode preparation were a mixture of 80 wt% active material, 10 wt% Carbon Black (C-NERGY Super C65, Imerys Graphite & Carbon, Bodio, Switzerland) and PVDF (Powerflex LBG1, Arkema, France) in N-methyl-2-pyrrolidone (NMP, Carl Roth) as solvent. Carbon-PVDF-NMP mixtures were prepared beforehand in a dissolver stirrer and preserved by constant shaking (KS-10, Edmund Bühler). Then the NMC active material was precisely weighted (AT261, Mettler-Toledo), added and mixed to the slurry with the help of a SpeedMixer (DAC S-150, Hauschild, Germany) for at least 5 min at 2000 rpm.

Electrodes were prepared by coating the slurry on a 12 μm thin Al-foil with the 200 μm slit of a manual film applicator (Erichsen Model 360, Germany) with the help of a programmed coating device (Erichsen Coater Model 510, Version 2.6, Germany). After coating, the electrodes were dried in air at 80 °C for 10 min on the coater, then at 110 °C for 24 h under vacuum (⩽5 mbar, VTR 5036, Heraeus).

After drying, cathode disks were punched out with a Ø 12 mm handheld punch (Nogamigiken, Japan), then compressed in a hydraulic press with a force of 6 kN for at least 20 s and once again dried for at least 3 h at 110 °C in the same oven as the coated electrodes. Usual cathode loadings thus obtained were in the range of 3.5–4.5 mg cm^{-2}. The cathodes were transferred under an argon atmosphere in an argon-filled glovebox (O_2 and H_2O ⩽0.1 ppm, MBraun, Germany) where the cells were built.

Cell assembly.—CR2032 coin cells made of SUS316L stainless steel (Hohsen Corp., Japan) were assembled with a Ø 16.5 mm Whatman GF/C Separator, 200 μl electrolyte and a Ø 15.6 mm lithium chip (Xiamen Tmax, China). The electrolyte used was a commercial 1.0 M $LiPF_6$ solution in 1:1 v/v ethylene carbonate: dimethyl carbonate (EC:DMC) (battery grade, Merck KGaA). A 1 mm thick spacer was used to ensure proper contact and stack height[31] and the cells were all closed at ≈650 psi in a hydraulic crimper (MSK-110, MTI Corp., USA). After closing, the cells were taken out of the glovebox and carefully cleaned with an isopropanol-soaked tissue to remove any residues of electrolyte. Cells tests were started directly after the cell assembly.

Cell test.—Electrochemical measurements were carried out via galvanostatic charge/discharge cycling at 1C-rate on an LBT20084 battery cycler (Arbin Instruments, College Station, TX, USA); 1 C being calculated based on the theoretical capacity of an actual cell with 0,66 Li exchanged per formula unit (e.g. 182.5 mAh g^{-1} for $LiNi_{0.6}Mn_{0.2}Co_{0.2}O_2$ ≡ 1 mAh for m_{AM} ≈ 5.48 mg). Cycling was performed in an air-conditioned room with a controlled temperature of 23 °C. A voltage window of 3–4.3 V vs Li^+/Li was applied, the cell internal resistance was checked at 3.7 V in the first cycle, then every 10 cycles. The first two cycles were used as formation cycles at charge and discharge rates of C/10. The coin cell tests were verified using at least three identically prepared cells. The variation between cells was less than 5%, typically around 2–3%.

Results and Discussion

Reference material.—Numerous samples of $Ni_{0.6}Mn_{0.2}Co_{0.2}(OH)_2$ were synthesized batch-wise under various conditions in a stirred tank reactor (STR), based on the widely used coprecipitation method.[32–34] Three goals were pursued to obtain the best in-house reference material for the following study of the impurities influence; secondary particles as spherical as possible, as less foreign ions as possible and a specific capacity of ≈150 mAh g^{-1} at 1 C. The pH-value, the suspension temperature and the stirring speed were well-known key parameters of

the coprecipitation synthesis to control the morphology of both primary and secondary particles.[35] Their fine tuning produced a deep dark brown powder (picture in Fig. S3) formed of the spheroids pictured in Figs. 1a, 1b. Those can be described as secondary or even tertiary particles, composed of very thin hexagonal platelets (Fig. 1c). The platelets are regrouped together in a mostly radial manner around one less dense nucleation core (Fig. S4), to form burgeons-like assemblies, themselves assembled in quite spherical agglomerates. These tertiary particles possessed a mean diameter close to 10 μm (d_{50} of 9.9 μm, as summed up in Table I), in good agreement from the size that can be roughly estimated from the SEM pictures (Figs. 1a, 1b). The narrow size distribution and regular spherical form certainly helped to produce the macroscopically fine, fluffy but compact powder obtained (no grinding needed after drying, $\rho_{geo} \approx 1.4\ g\ cm^{-3}$).

Special care was also exerted on other parameters of the coprecipitation synthesis, to get a reference material as pure as possible. Specifically, the presence of the N_2-flux and the limitation of the overnight drying step at only 80 °C under air were crucial, both allowing to avoid the unwanted oxidation of the hydroxide into a $Ni_{0.6}Mn_{0.2}Co_{0.2}OOH$ oxyhydroxide.[36] Phase identification of the crystal structure of the synthesized $Ni_{0.6}Mn_{0.2}Co_{0.2}(OH)_2$ (Fig. 2, top) yielded a single-phased product with a layered CdI2-type structure (SG: $P\bar{3}m1$).[37] As noticeable on Fig. 2, the reflections in the hydroxide XRD pattern were quite broadened with low intensities, pointing towards the presence of defects, like the stacking faults and turbostratic phase observed on similar materials.[38,39] Based on such diffraction data, the pattern refinement was limited to profile matching (Fig. 2, top-right), yielding reasonable cell parameters, in good agreement with the reference found in the ICSD Database[40] (Table III). At last, it was not possible to completely rule out the presence of the oxyhydroxide phase, but its amount was certainly not significant: otherwise, new reflections should have arisen, as observed for harsher drying conditions and highlighted in Fig. S5.

ICP-OES analyses were undertaken to assess the final composition of the synthesized hydroxide and to detect any other element present in it. The expected stoichiometry was reproducibly achieved: $Ni_{0.60}Mn_{0.20}Co_{0.20}(OH)_{2.2}$, the eventual deviations between Ni, Mn and Co amounts being smaller than the measuring inaccuracy (one example of ICP-OES results, standard deviations and measuring errors is displayed in Table S1). Please note that the determination of the oxygen amount is the most inaccurate of all tested elements (e.g. 36.4 ± 3.0 wt% for the hydroxide reference material), leading to the offset stoichiometric amount given here above. Some foreign ions were detected and are listed in Table II. The presence of nitrogen, sulfur and sodium is not unexpected, due to the use of ammonium and sodium hydroxide solutions in the coprecipitation reaction. The sulfur amount is related to residual sulfate molecules trapped in the core of the tertiary particles and between the hydroxide primary particles.[41] The detection of silicon and boron was attributed to abrasion of the glass reactor, especially given its intensive use by high pH-values, whereas carbon was linked to CO_2 contamination during storage. Lastly, some aluminium was incorporated in the hydroxide, most probably due to its presence in the precursors, its amount staying below the smallest concentration studied in this work, i.e. 0.01 at%. Interestingly, only the amount of nitrogen was reduced for the reference material washed 8 times, compared to a sample washed only 4 times (Table S2), even if a prolonged washing had a positive impact on the cell capacity, as shown later.

Further modifications of the synthesis parameters let tailor the morphology further, as depicted in Fig. S6, but more regular spheres with a smooth surface[42] were not within the reach of the laboratory set-up used, especially regarding the stirring speed.[43] Therefore, this hydroxide reference material was deemed sufficient for studying the impurity impact and ultimately characterized by N_2 adsorption and Hg intrusion to determine its specific surface and porosity (Table III).

The second step of the CAM synthesis was the mixing of the precursor with the Li-source, which was thought to insure a homogenous mixing with the hydroxide, while keeping its morphology and being scalable. Such objectives ruled out the hand mixing practiced otherwise at laboratory scale and led to the use of other techniques and devices, like the mortar grinding or the ball-mill. Only the later brought the expected result at low milling energy, as shown by the comparison of the SEM top views in Fig. 3 for milling speeds of 300 rpm (left, all agglomerates destroyed) and 100 rpm (right, morphology well maintained). Finally, the cell capacity obtained during galvanostatic cycling at a 1C-rate was the highest for the material obtained after mixing at 100 rpm, as pictured in Fig. S7.

Calcinating the mixture was undertaken in a two-step process, to account for the slow lithiation kinetics of Li_2CO_3[44] and avoid the presence of too much voids and pores, as advised by studies probing this reaction in situ for NMC 622[45] and similar Ni-rich materials.[46] The resulting product is composed of secondary particles being roughly spherical agglomerates of primary particles having mostly a thick platelet-like form (Figs. 1d–1f), with largely dominant (001)-crystal facets.[47] As also shown by the little changes in particle size distribution (Table I), the synthesis design led to the preservation of the overall particle morphology. The small size decrease can be

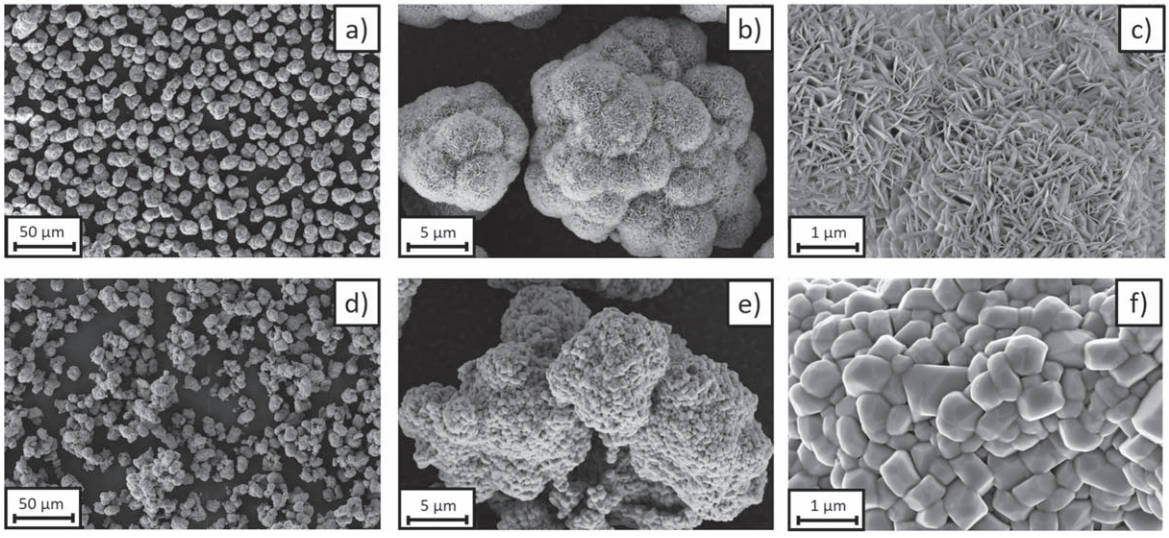

Figure 1. SEM top-view of the $Ni_{0.6}Mn_{0.2}Co_{0.2}(OH)_2$ (a)–(c) and $LiNi_{0.6}Mn_{0.2}Co_{0.2}O_2$ (d)–(f) reference material at increasing magnification (from left to right).

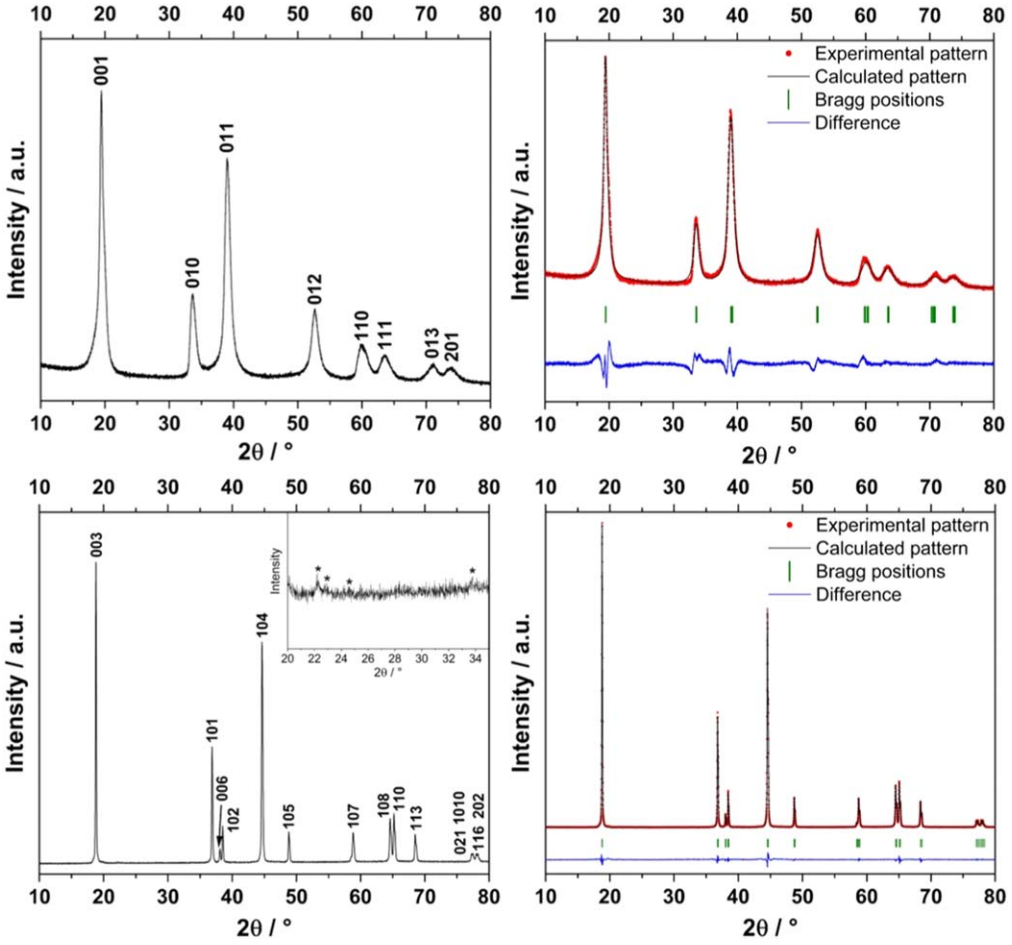

Figure 2. PXRD patterns (left) of the $Ni_{0.6}Mn_{0.2}Co_{0.2}(OH)_2$ (top) and $LiNi_{0.6}Mn_{0.2}Co_{0.2}O_2$ (bottom, with a zoom on the 20–37° 2θ domain in the inset, stars indicating the presence of a minor impurity) in-house reference materials and corresponding Le Bail refinements (right).

Table I. Volumetric particle size distribution of the reference materials, based on laser scattering measurements.

Particle size (μm)	$Ni_{0.6}Mn_{0.2}Co_{0.2}(OH)_2$	$LiNi_{0.6}Mn_{0.2}Co_{0.2}O_2$
$d_{10,3}$	6.3	5.7
$d_{50,3}$	9.9	8.7
Mode	10.7	9.4
$d_{90,3}$	14.7	13.1

attributed to particle compaction, in light of the strong decrease of the porosity, compared to the hydroxide (Table III). The concomitant strong reduction of the specific surface area should reduce the absolute discharge capacity at start but should be an advantage regarding capacity retention. Just as for the hydroxide, the purity goal was assessed firstly by the characterization of the crystal structure, then by the determination of the elemental composition.

As seen in Fig. 2 (bottom), the PXRD pattern of the oxide reference material displayed an almost single-phased product with a layered α-$NaFeO_2$-type structure (SG: $R\bar{3}m$). A very good match between the experimental and calculated diagrams was observed with low reliability factors when conducting profile matching refinements of this PXRD pattern (Fig. 2, bottom-right), which yielded cell parameters very close to the ones reported[40] in the ICSD Database (Table III). The expected $LiNi_{0.6}Mn_{0.2}Co_{0.2}O_2$ phase was then successfully synthesized and displayed a clear splitting of (006)/(102) and (018)/(110) reflections, indicator of a good hexagonal ordering,[48] and a I_{003}/I_{104} ratio clearly superior to 1.2 (≈1.41), a strong hint towards a low amount of Li^+/Ni^{2+} cation mixing.[49] Only a zoom in the 20–35° 2θ domain revealed a very small amount of what was tentatively identified as a lithium sulfate silicate phase ($Li_{16}(SiO_4)_3(SO_4)_2$, PDF-File #00–038–1476). The intensity of these reflections stayed very small (i.e. ≈0.38% of the main (003) reflection) but was constant throughout the reproduction

Table II. Impurity content for both reference materials, based on the results of elemental analysis.

$Ni_{0.6}Mn_{0.2}Co_{0.2}(OH)_2$

Impurity	N	C	S	Si	B	Na	Al
at%	0.65	0.40	0.22	0.12	0.012	0.007	0.005
wt%	0.31	0.16	0.23	0.11	0.004	0.006	0.005

$LiNi_{0.6}Mn_{0.2}Co_{0.2}O_2$

Impurity	N	C	S	Si	B	Na	Al	Zr
at%	0	0.03	0.14	0.09	0.009	0.009	0.03	0.002
wt%	0	0.02	0.18	0.10	0.004	0.009	0.03	0.008

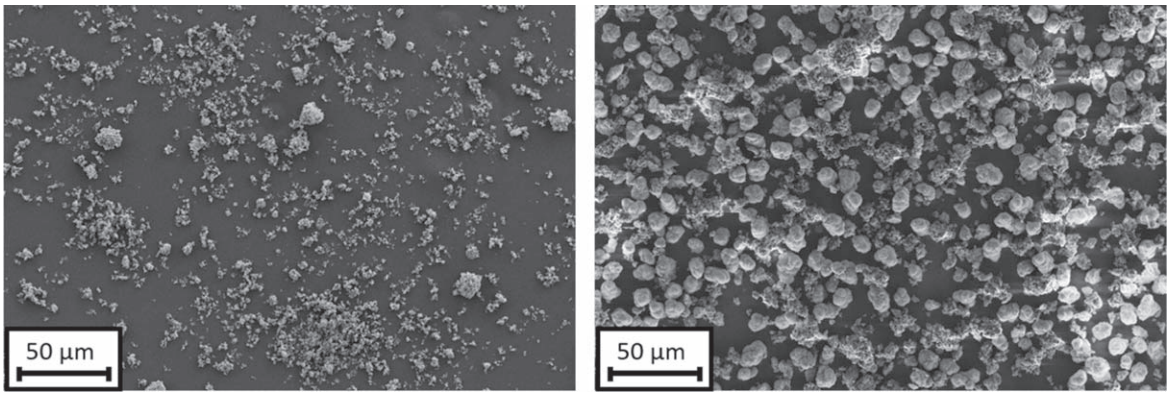

Figure 3. SEM top-view of the $Ni_{0.6}Mn_{0.2}Co_{0.2}(OH)_2$ reference material mixed in a planetary ball mill with Li_2CO_3 at 300 rpm (left) and 100 rpm (right) at similar magnification.

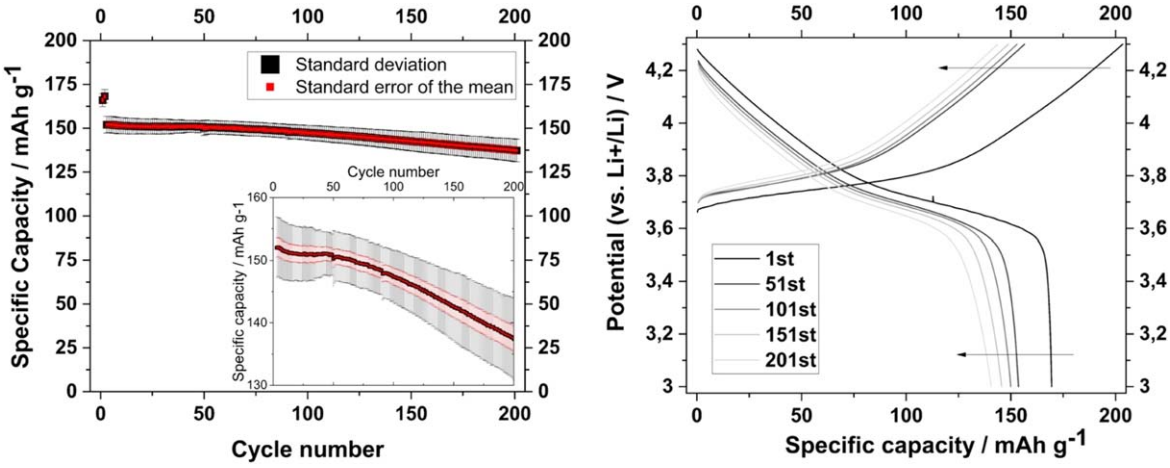

Figure 4. Evolution of the discharge capacity of the $LiNi_{0.6}Mn_{0.2}Co_{0.2}O_2$ reference material against Li in coin cells in function of the cycle number (left-with a zoom in inset) and of the corresponding charge/discharge profile of a representative cell (right). The first two cycles were conducted at 0.1 C and the following 200 cycles at 1 C; the arrows indicate the direction of the cycle number increase. NB: the spikes in the voltage profile at 3.7 V are due to the internal resistance test.

Table III. Physico-chemical data of the reference materials.

Reference material	Hydroxide	Oxide
Cell parameters (Å)	a = 3.1084(6)	a = 2.86780(3)
	c = 4,609(3)	c = 14,2179(2)
Specific surface area ($m^2\ g^{-1}$)	17.1	0.4
Porosity (%)	26.3	<2

of the reference material batches. It was at least clear that these minor impurities were no Li_2CO_3 which would have come from air contamination and no sulfates precursors leftovers.

The results of the elemental analysis of the oxide reference material let determine the experimental stoichiometry of $Li_{1.05}Ni_{0.60}Mn_{0.20}Co_{0.20}O_{2.2}$ and let quantify the amount of foreign ions, as listed in Table II. Compared to the hydroxide, the calcination step helped to get rid of the nitrogen leftovers, as well as of an important part of the carbon atoms and of some sulfur ones, whereas the quantity of silicon, boron and sodium underwent only small changes. Important to notice was the detection of zirconium coming from the jar and ball material of the ball-milling step, and the six times multiplication of the aluminium amount. The cause of this increase was a contamination coming from the calcination boat made of Al_2O_3, up to a concentration higher than the smallest Al-concentration studied in this work, and observed in all of the calcinated samples. Finally, the composition of the impurity detected in XRD was corroborated by the detection of sulfur and silicon with ICP-OES and some observations made while studying cross-sections of electrodes coated with this CAM. As shown in Fig. S8, a few molten-like regions close to the NMC 622 particles were observed and their characterization via EDX revealed an elemental composition rich in silicon, sulfur and oxygen. The amorphous appearance of this phase would corroborate well with its very low XRD reflection intensity.

The last characterization of the oxide reference material was conducted in coin cells against lithium metal. These half-cells first undertook two formation-like cycles at 0.1 C and were then galvanostatic cycled at 1 C between 3 and 4.3 V for 200 cycles. Their cycling performance as well as typical voltage profiles were pictured in Fig. 4, when their internal resistance and coulombic efficiency data were plotted in Fig. S9. To minimize the influence of cell building[31] and of the cycling device on data accuracy, the oxide reference material was probed two times and sampled three times, i.e. three separate rows of three cells out of two different coatings were punched out and 18 cells were cycled. The discharge capacity points presented in Fig. 4 were the calculated mean value for the 18 cells. The standard deviation error bars indicate the maximum dispersion observed during these tests and the standard error of the mean error bars indicate the dispersion domain of the mean discharge capacity value (≈156 mAh g^{-1} after 10 cycles). The cell

Table IV. Summary and translation of the planed impurity concentrations.

Impurity concentration	Small	Middle	High
x in $Ni_{0.6}Mn_{0.2}Co_{0.2}M_x(OH)_2$	0.0005	0.005	0.05
Atomic fraction (at%)	0.01	0.1	1.0
Weight fraction (wt%)			
Al	0.015	0.15	1.5
Fe	0.030	0.30	3.0
Li	0.004	0.04	0.4

internal resistance was quite low at the beginning of the cycling (≈18 Ω cm^2), before following a S-like curve with a linear increase up to the 80th cycle, a dwell of 100 cycles and a new increase to ≈32 Ω cm^2 afterwards. This was partly mirrored by a concomitant decrease of the coulombic efficiency from ≈99.5% to ≈98% during the first 80 cycles, with no noticeable evolution afterwards. At the end of the cycling test, the capacity retention was about 90%, making the electrochemical performances of this reference material a good match to the ones reported by similar studies on NMC 622.[23–27] As mentioned previously, optimizing the washing step at the end of the coprecipitation did not induce noticeable changes in the elemental composition (Table S2) but did improve the discharge capacity value (Fig. S10). Trying to increase the specific capacity by increasing the active material loading or the Li extraction rate only led to faster dendrite growth and cell failures issues. The mean start discharge capacity of ≈155 mAh g^{-1}@1 C thus obtained was the one used as a standard in the following part of this study.

Impurities influence.— *Morphology.*—Carefully preparing a reference material allowed to look for the smallest and most diverse influences of the impurities. For each impurity, namely Al, Fe and Li as M in $Ni_{0.6}Mn_{0.2}Co_{0.2}M_x(OH)_2$, three concentrations were tested (Table IV) by introducing the corresponding hydrated sulfates in the transition metal feeding solution used for the coprecipitation synthesis. The x values were translated into atomic and weight fraction to allow for a more straightforward comparison with other works, according to the reader's background.

Compared to similar studies, the concentration domain in this work is quite analogous to the one chosen for Al and Fe in NMC 111[23,25] and a bit lower to the one chosen for Li in NMC 111[27] and Al and Fe for NMC 622[24,26]; 1.0 at% being considered the threshold for doping. Given the importance of the morphology on the CAM performances,[35] it was the first characteristic of the hydroxide to be looked upon in the presence of the impurities, as displayed in Fig. 5. The SEM pictures of the pCAM synthesized with increasing amount of Al showed its visible effect on the morphology of the particles. By the smallest amount, the primary and tertiary particles tended to be identical to the reference material (Figs. 5a, 5d), but already at x = 0.005, some differences emerged in the size and at the surface of the agglomerates (Figs. 5b, 5e), which then lost their sphericity almost completely at x = 0.05. At this high concentration (Figs. 5c, 5f), it could be noticed that the primary particles were prone to constitute small assemblies, especially at the surface of the tertiary particles. This is in good agreement with the increased irregularity of the particle shape that was observed previously[23] and can be corroborated by studies on the coprecipitation synthesis of Ni-Co-Al (NCA) hydroxides: $Al(OH)_3$ precipitates readily by pH = 11, which favorizes the formation of a large number of nuclei over the growth of bigger particles.[50–52]

Such dramatic changes of the particle morphology were not observed during syntheses in presence of Fe or Li, as can be sighted in Fig. S11. Some slight disturbances were spotted on the surface of the agglomerates at x = 0.05 with kind of small offshoots for both Fe and Li. Nevertheless, it was difficult with such a low impact to discriminate between the impurities influence and the one due to variations of pH-value or temperature naturally occurring between each batch. This assumption was supported by the inner view of the tertiary particles (Fig. 6), which were almost identical to the reference material (Fig. S4) for both Fe and Li, in contrary to the Al case. The highest concentration of aluminium totally disturbed the normal growth of the agglomerates with even some dense filaments partially surrounding the regular platelet-like primary particles. A first estimate of the composition of such ribbons via EDX mapping suggested the concomitant presence of Ni and Al, as exposed in Fig. S12.

The evolution of further morphology-related material properties was shown in Fig. 7 for all hydroxides: tertiary particle size, specific surface area and porosity (the actual values are listed in Table S3). At low and middle impurities concentrations (x = 0.0005 and 0.005), these properties were all analogous to the values obtained for the reference material, i.e. a d_{50} value close to 10 μm with a quite narrow size distribution, a porosity value close to 26% and a specific surface area comprised between 16 and 20 m^2 g^{-1}. Only when reaching x = 0.05 became the Al influence remarkable again: just as suggested from the SEM pictures, the particle size distribution in presence of 1 at% of aluminium was largely increased, ranging from 2 to 28 μm. Following the disturbed morphology, the corresponding porosity and specific surface area showed a parallel increase to ≈42% and ≈30 m^2 g^{-1}, respectively. On the contrary, the effects of Fe and Li were much restrained and could also solely be related to measurements limitations: just a slight increase in porosity in the iron case, from ≈26 to ≈30% and an extension of the specific surface area from 16 to 23 m^2 g^{-1} with lithium. As a last note regarding the morphology, the $Ni_{0.6}Mn_{0.2}Co_{0.2}Al_{0.05}(OH)_2$ powder's hardness increased noticeably, rending it much complicated to grind after drying, and its apparent density dropped to $\rho_{geo} \approx 0.8$ g cm^{-3}. This was not observed in the Fe nor Li case.

As was expected from the soft conditions of ball milling and already demonstrated for the reference material, the morphological evolutions were maintained after calcination, as displayed in Fig. S13. Almost the same tertiary particles size values were measured, compared to the corresponding hydroxides, and the specific surface area and porosity values were almost zero (Table S3), due to the compactness of the oxides agglomerates and the smooth surface of their primary particles. If the mixing and calcination part is optimized enough, the determining effects of impurities will then appear during coprecipitation and be kept throughout the whole further process.

Composition.—Using ICP-OES analysis, the stoichiometric amount of the main elements of all samples was calculated and listed in Table V. One important result of these measurements was the total absence of lithium (at least above the detection limit) in the hydroxides samples synthesized with Li_2SO_4 in the TM solution. The lithium was not precipitated along with Ni, Mn and Co, probably due to the very high solubility of LiOH in water, and was then washed away after the sample collection, as already observed by Jo et al.[27] On the contrary, Fe was found in the same quantity as what was introduced as reactant and Al too, with the addition of the aluminium naturally present in our set-up and already detected in the reference material (Table II). Taking the Co amount as reference just like in the work of Zhang et al.[24] the Co:Mn:Ni ratio in the hydroxides did not evolve far from the expected 1:1:3, be it with increasing Al (1:1.00:2.93; 1:1.00:2.96; 1:1.00:2.97) or Fe amount (1:1.01:2.94; 1:1.01:2.95; 1:0.99:2.97). Based on these data and regarding the measurement uncertainty, it was only possible to conclude that Al and Fe were effectively incorporated in the materials but not to reveal any loss of Ni, Mn or Co.

Crystal structure.—All the PXRD patterns of the hydroxides and oxides synthesized in presence of Al, Fe or Li were compared to the ones of the reference material in Fig. 8. At first glance, the crystal

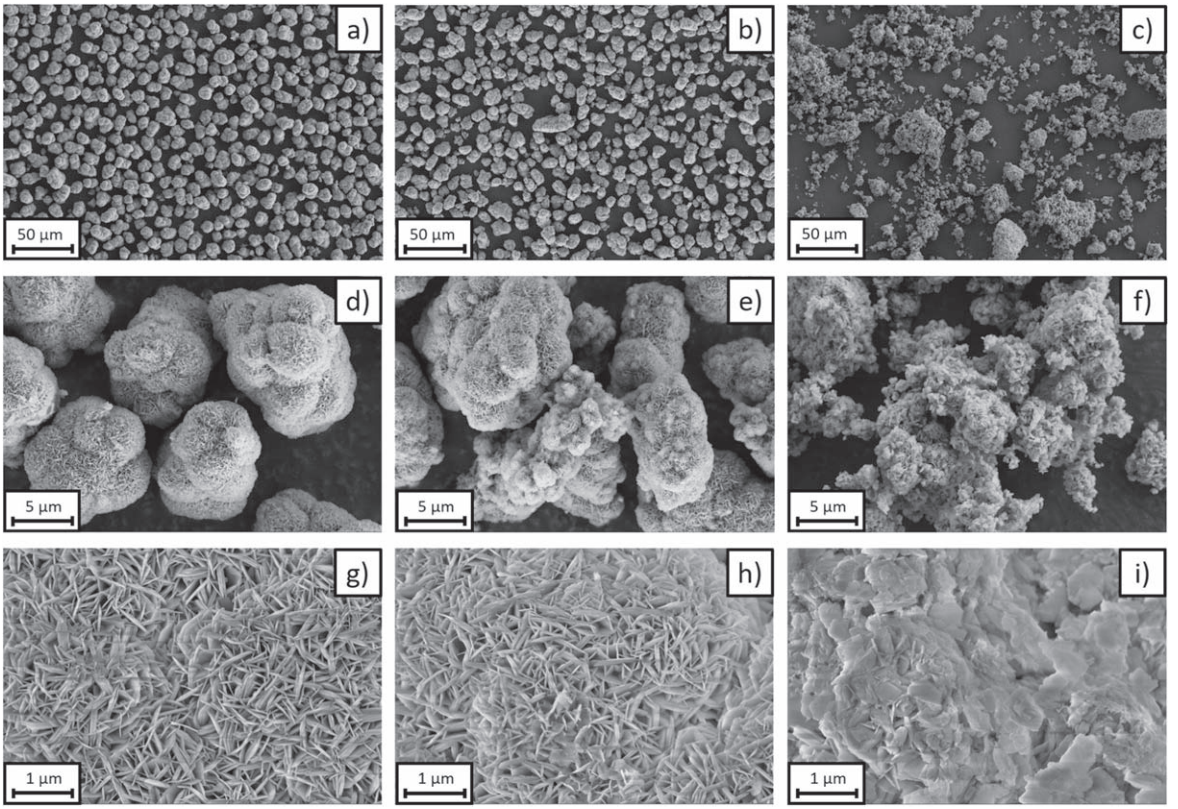

Figure 5. SEM top-view of the $Ni_{0.6}Mn_{0.2}Co_{0.2}Al_{0.0005}(OH)_2$ (left, (a)–(d)–(g)), $Ni_{0.6}Mn_{0.2}Co_{0.2}Al_{0.005}(OH)_2$ (middle, (b)–(e)–(h)) and $Ni_{0.6}Mn_{0.2}Co_{0.2}Al_{0.05}(OH)_2$ (right, (c)–(f)–(i)) materials at increasing magnification (from top to bottom).

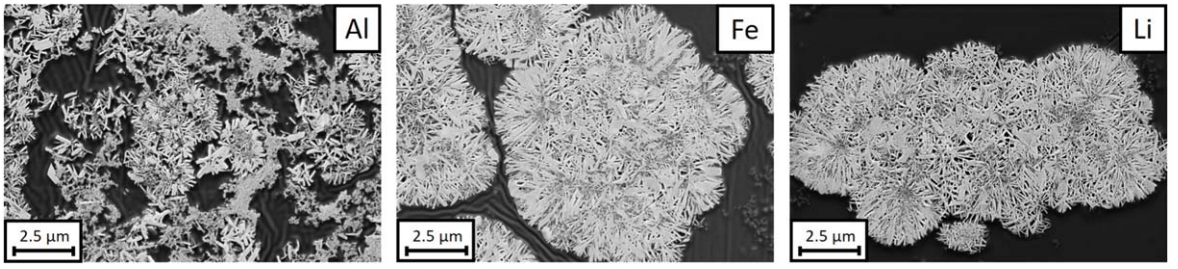

Figure 6. SEM cross-section images of the $Ni_{0.6}Mn_{0.2}Co_{0.2}M_{0.05}(OH)_2$ hydroxide with M = Al, Fe or Li at similar magnification.

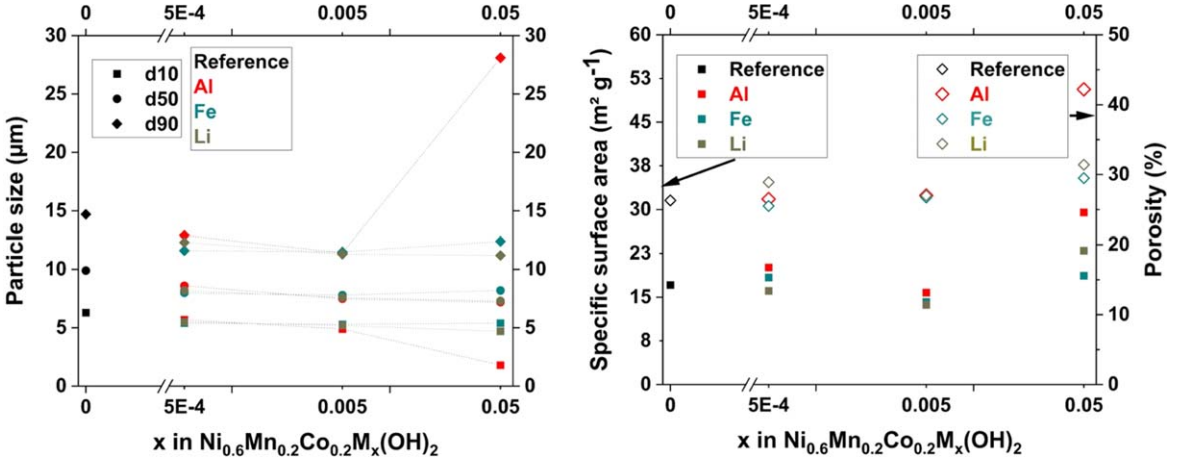

Figure 7. Evolution of the tertiary particle size (left), of the specific area and of the porosity (right) of all hydroxides. the dashed lines in the particle size figure are a reading help and do not aim to represent any linear evolution.

Table V. Chemical formula of all the materials synthesized in presence of Al, Fe or Li, based on results of elemental analysis.

Al	Fe	Li
$Ni_{0.59}Mn_{0.20}Co_{0.20}\mathbf{Al_{0.0007}}(OH)_{2.3}$ $Li_{1.04}Ni_{0.59}Mn_{0.20}Co_{0.20}\mathbf{Al_{0.0014}}O_{2.1}$	$Ni_{0.59}Mn_{0.20}Co_{0.20}\mathbf{Fe_{0.0005}}(OH)_{2.2}$ $Li_{1.02}Ni_{0.59}Mn_{0.20}Co_{0.20}\mathbf{Fe_{0.0005}}O_{2.1}$	$Ni_{0.60}Mn_{0.20}Co_{0.20}\mathbf{Li_{0.0000}}(OH)_{2.2}$ $Li_{1.07}Ni_{0.60}Mn_{0.20}Co_{0.20}O_{2.2}$
$Ni_{0.60}Mn_{0.20}Co_{0.20}\mathbf{Al_{0.005}}(OH)_{2.3}$ $Li_{1.06}Ni_{0.59}Mn_{0.20}Co_{0.20}\mathbf{Al_{0.006}}O_{2.1}$	$Ni_{0.59}Mn_{0.20}Co_{0.20}\mathbf{Fe_{0.005}}(OH)_{2.2}$ $Li_{1.06}Ni_{0.60}Mn_{0.20}Co_{0.20}\mathbf{Fe_{0.005}}O_{2.2}$	$Ni_{0.59}Mn_{0.20}Co_{0.20}\mathbf{Li_{0.000}}(OH)_{2.2}$ $Li_{1.04}Ni_{0.60}Mn_{0.20}Co_{0.20}O_{2.1}$
$Ni_{0.60}Mn_{0.20}Co_{0.20}\mathbf{Al_{0.05}}(OH)_{2.6}$ $Li_{1.18}Ni_{0.60}Mn_{0.20}Co_{0.20}\mathbf{Al_{0.05}}O_{2.4}$	$Ni_{0.60}Mn_{0.20}Co_{0.20}\mathbf{Fe_{0.05}}(OH)_{2.3}$ $Li_{1.09}Ni_{0.60}Mn_{0.20}Co_{0.20}\mathbf{Fe_{0.05}}O_{2.2}$	$Ni_{0.60}Mn_{0.20}Co_{0.20}\mathbf{Li_{0.00}}(OH)_{2.2}$ $Li_{1.06}Ni_{0.60}Mn_{0.20}Co_{0.20}O_{2.2}$

structure of the pCAM remained unchanged at the exception of the highest Al concentration, which showed the presence of a second crystalline phase. These new reflections could be attributed to a jamborite-like phase,[53] also reported as a layered double hydroxide (LDH) phase, an issue that was commonly observed during unoptimized synthesis of NCA hydroxides.[54,55] This new phase is preferentially stabilized in presence of trivalent cations and of sulfate anions, which is consistent with the introduction of $Al_2(SO_4)_3$ and with the elemental identification obtained via EDX, as presented in Fig. S12. A closer look on the other patterns revealed only limited reflections shifts in the case of Fe, as well as some modifications of the reflections intensities, even in the case of Li (Fig. S14). The small perturbation of the first reflection (001) suggested a limited impact on the interlayer distance, whereas the strong intensity changes of the second and third reflections (010 and 011, respectively) hinted for an influence on the TM layer constitution and orientation.[38] If this was deemed possible because of an actual incorporation of Fe in the hydroxide as thought after the ICP-OES results, it was more unexpected in the Li experiments, due to its absence after washing. Given that the reflections intensity increased along with Li_2SO_4 amount in the TM solution, its presence could be having some kind of discreet templating effect, before being washed away.

After calcination, all of the oxides displayed a single-phased PXRD pattern with the layered α-$NaFeO_2$-type structure (SG: $R\bar{3}m$) obtained for the reference material, even in the case of the highest Al concentration. Compared to the pure NMC 622, the clear splitting of (006)/(102) and (018)/(110) reflections was maintained, indicating no major effect of the impurities on the hexagonal ordering of the structure (Fig. 8c). Looking at the erratic increase of the I_{003}/I_{104} ratio (Table VI), the cation mixing could be slightly decreased[49] in the case of Al and Li and possibly at the lowest Fe concentration, just as suggested in similar works.[24,26] To confirm this hypothesis, more detailed structural characterizations will be performed and presented in a separate publication. A shift of the main reflections to lower angles was mainly observed in the presence of iron and essentially at the highest concentration (Fig. 8d), as already highlighted by Park et al.[25] and Zhang et al.[26] indicating a possible increase of the *c* cell parameter and of the linked interlayer distance. This assumption was supported by the results of profile matching refinements, yielding the cell parameters listed in Table VI. The *a* and *c* parameters were both increased by the introduction of Fe, especially when reaching x = 0.05, whereas *a* decreased when *c* increased in the Al case, in good agreement with previous similar studies.[23,24] The good conservation of the layered structure was marked by the almost constant c/a ratio throughout the whole impurities range.[56,57] All these evolutions pointed towards an incorporation of aluminium and iron at first into the TM layer and then between the layer for Fe[26] at x = 0.05. The absence of lithium in the hydroxides naturally led to XRD patterns (Fig. S14d) and structural parameters close to the reference oxide material, possibly slightly different because of the templating discussed for the hydroxide.

Electrochemistry.—Just as for oxide the reference material, the contaminated oxides were tested as CAM in coin cells against lithium metal. These half-cells first undertook two formation-like cycles at 0.1 C and were then galvanostatic cycled at 1 C between 3 and 4.3 V for 200 cycles. For the specific discharge capacity date, the standard error of the mean of a row of three cells was considered; the reproducibility of each row was tested once, the deviation of discharge capacity data having been verified with the reference material. The cycling performance as well as typical voltage profiles and differential capacity evolutions were pictured in Fig. 9 for Al and Fe, when all the internal resistance and coulombic efficiency data were plotted in Fig. S15. The voltage profiles and differential capacity plots were extracted at the 51st cycle, rather than at a previous or later cycle to avoid as well as possible any disturbance from the cell individuality, the cell formation or a pronounced cell aging. The corresponding diagrams for Li were regrouped separately, because the absence of lithium and its only subtle modifications of the CAM compared to the reference material led to almost unchanged data and curves, as can be observed in Fig. S16. This allowed to use the Li case as a kind of benchmark to try to discriminate between the influence of the impurities and the one of the slurry- or cell-making. Indeed, even if the discharge capacity values of the cells with Al and Fe at x = 0.0005 and 0.005 slightly decreased compared to the ones with pure NMC 622 (Figs. 9a, 9b), their voltage profiles and differential capacity curves were fast identical to the ones of the reference material (Figs. 9c–9f). Only at x = 0.05/1 at%, similar phenomena were identified: a noticeable drop in the absolute discharge capacity values, a decrease in charge and discharge capacity and a shift and change of the redox peaks. The magnitude of these changes was higher in the Fe case than in the Al case and accompanied by a decreased capacity retention (≈85% vs 90% in all other cases).

These findings would suggest that the incorporation of electrochemically inactive Al^{3+} decreased the reachable capacity and that the presence of a too high amount of Fe^{2+} exacerbated the electrode polarization, thus making the reversible (de)lithiation more difficult. This is to a great extent in line with previous observations on NMC 111 and 622, especially regarding the Al concentration and the Fe valence. According to Kim et al.[23] the Al electrochemical impact threshold was found between 0.05 at% and 0.25 at% and between 0.1 at% and 1 at% in this work. A trivalent iron would have led to much faster electrochemical degradation as what was observed here and similarly with Fe^{2+} by Zhang et al.[26] Nonetheless, a careful look at the results of the elemental analysis showed the presence of a large Li excess at the highest Al and possibly Fe concentration (Table V), caused by the influence of the impurities on the pCAM quality. This could also lead to lower capacity values,[58,59] so that the Li-excess influence should be thoroughly compared to the sole addition of impurities in further studies. Finally, no positive effects at all on the capacity values were observed in this study, even at the lowest impurity concentration, in contrary to what was inferred in similar works.[24,25] As displayed in Fig. S15, rate capacity tests were performed with one extra cell for each row of Al, Fe, Li cells; the discharge capacity values were close the ones of the 1 C cycling tests and demonstrated no substantial improvement of the rate capacity. A capacity increase was suggested at low C-Rates for $x_{Fe} = 0.005$ and at 10 C for $x_{Al,Fe} = 0.0005$ (Fig. S17), but remained very doubtful, due to its low magnitude and because occurring also in some cells

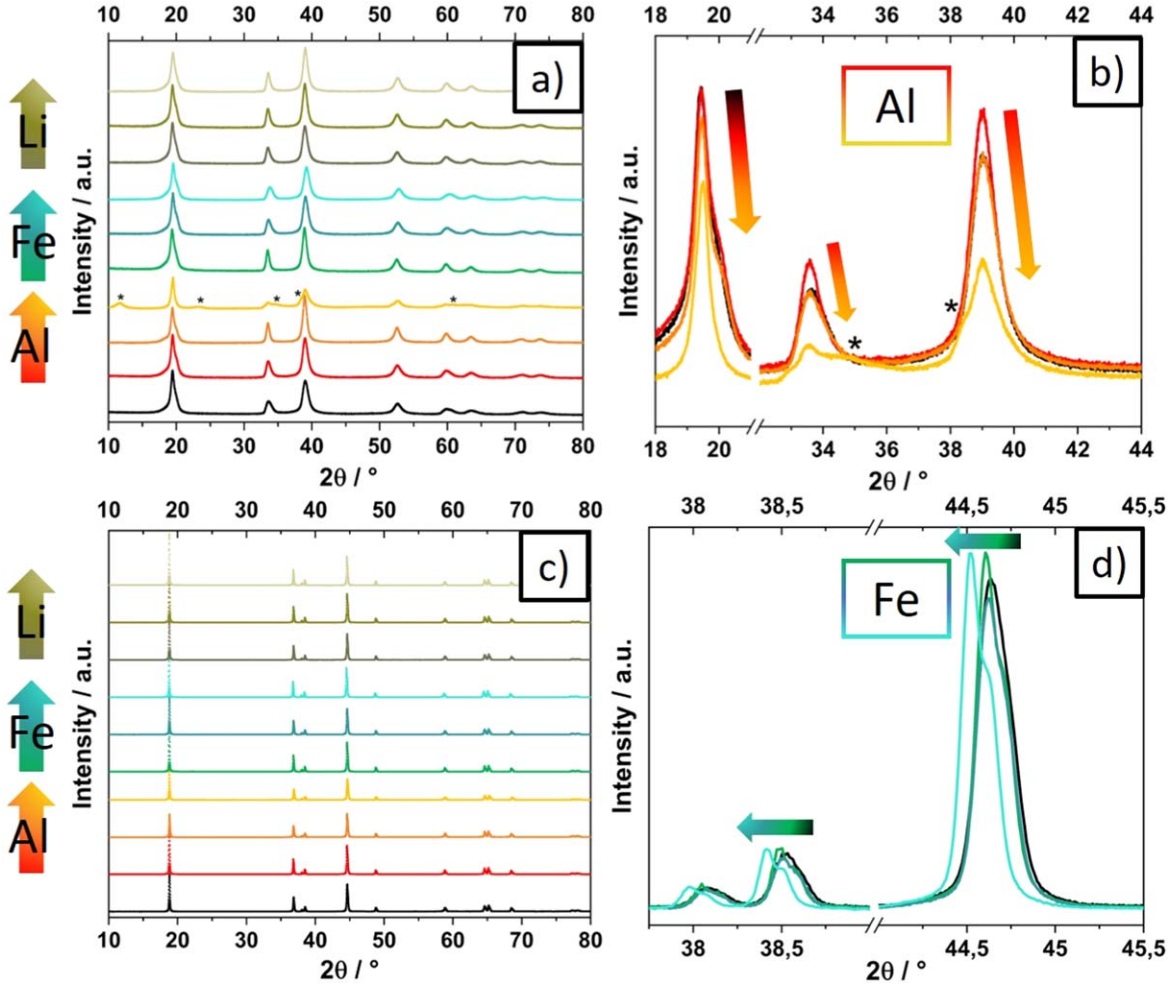

Figure 8. PXRD patterns of $Ni_{0.6}Mn_{0.2}Co_{0.2}M_x(OH)_2$ with M = Al, Fe, Li and x = 0.0005, 0.005, 0.05 (a) and corresponding $LiNi_{0.6}Mn_{0.2}Co_{0.2}M_xO_2$ (c), with zooms on the 18–44° 2θ domain for Al-contaminated hydroxides (b) and on the 37,5–45,5° 2θ domain for Fe-contaminated oxides (d). The stars indicate the presence of a second phase (jamborite/LDH-like) in $Ni_{0.6}Mn_{0.2}Co_{0.2}Al_{0.05}(OH)_2$. The reference hydroxide (a)–(b) and oxide (c)–(d) patterns are plotted in black. The arrows are a help for the eyes, to follow the concentration-related changes (concentration increase from dark to pale).

Table VI. Structural parameters of the oxides synthesized in presence of Al, Fe and Li, compared to the reference CAM, obtained after profile matching refinements of the corresponding PXRD patterns.

Composition	I_{003}/I_{104} ratio	Cell parameter (Å)		c/a
		a	c	
$LiNi_{0.6}Mn_{0.2}Co_{0.2}O_2$	1.41	2.86780(3)	14.2179(2)	4.9613
$LiNi_{0.6}Mn_{0.2}Co_{0.2}Al_{0.0005}O_2$	1.45	2.86745(3)	14.2192(3)	4.9588
$LiNi_{0.6}Mn_{0.2}Co_{0.2}Al_{0.005}O_2$	1.44	2.86631(3)	14.2195(3)	4.9609
$LiNi_{0.6}Mn_{0.2}Co_{0.2}Al_{0.05}O_2$	1.52	2.86296(3)	14.2224(3)	4.9677
$LiNi_{0.6}Mn_{0.2}Co_{0.2}Fe_{0.0005}O_2$	1.64	2.86653(3)	14.2204(4)	4.9608
$LiNi_{0.6}Mn_{0.2}Co_{0.2}Fe_{0.005}O_2$	1.42	2.86752(3)	14.2258(3)	4.9610
$LiNi_{0.6}Mn_{0.2}Co_{0.2}Fe_{0.05}O_2$	1.50	2.87190(3)	14.2470(3)	4.9608
$LiNi_{0.6}Mn_{0.2}Co_{0.2}Li_{0.0005}O_2$	1.45	2.86636(3)	14.2217(3)	4.9616
$LiNi_{0.6}Mn_{0.2}Co_{0.2}Li_{0.005}O_2$	1.56	2.86613(3)	14.2199(4)	4.9614
$LiNi_{0.6}Mn_{0.2}Co_{0.2}Li_{0.05}O_2$	1.77	2.86708(3)	14.2180(4)	4.9591

built with the Li-contaminated CAM. With Li as an impurity, the oxidation peak intensity increased with the lithium sulfate concentration, along with the low effects noticed on the hydroxides and oxides structure, but this had no peculiar impact on the achievable discharge capacity (Fig. S16). The fact that the middle Li-impurity concentration showed slightly lower specific capacity values ($\approx$5 mAh g^{-1}) as the low and high concentrations was more probably a cautious recall of the influence of the cell fabrication and testing than a real effect of the Li_2SO_4 presence in the coprecipitation reaction.

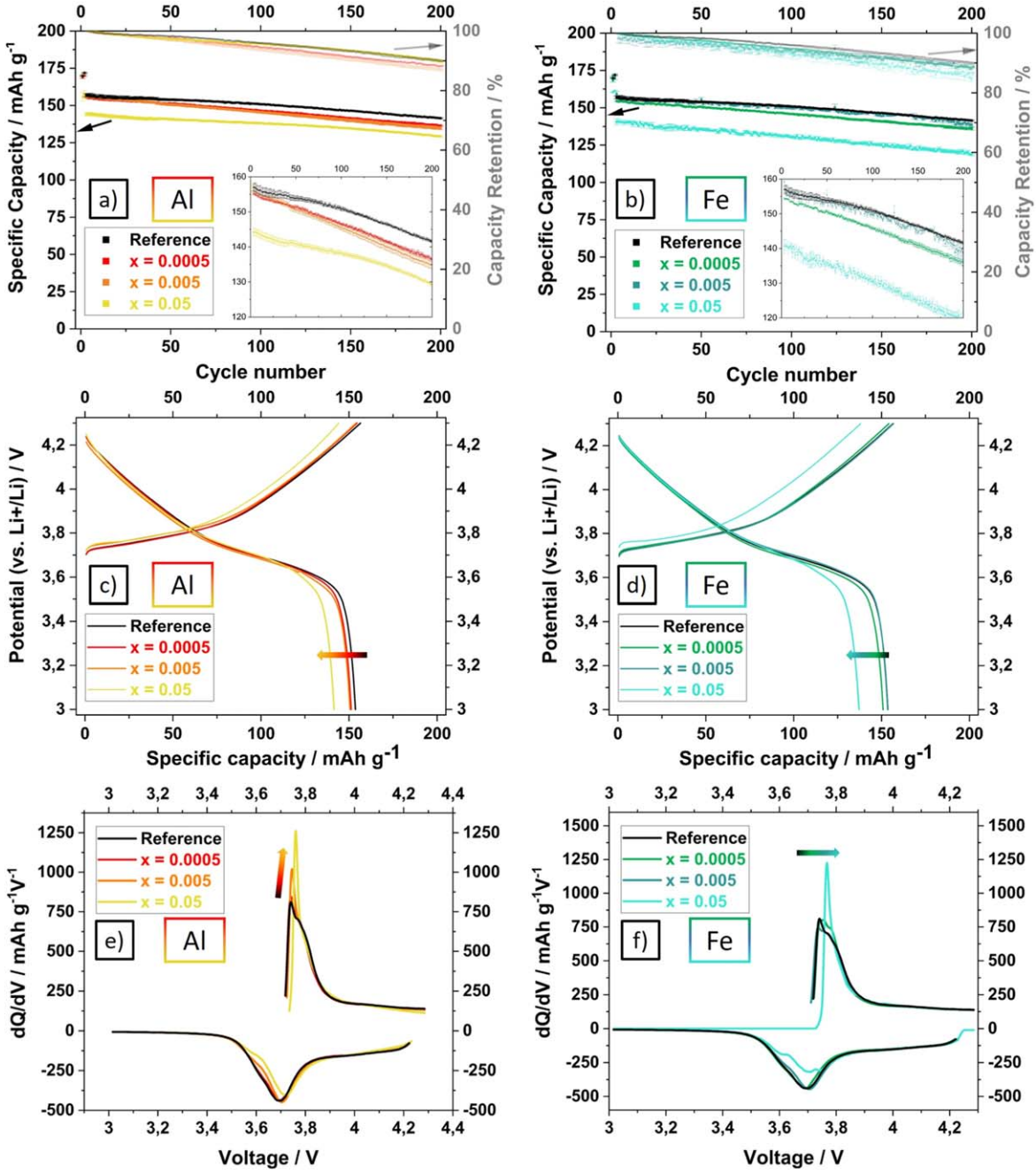

Figure 9. Evolution of the discharge capacity of $LiNi_{0.6}Mn_{0.2}Co_{0.2}Al_xO_2$ (a) and $LiNi_{0.6}Mn_{0.2}Co_{0.2}Fe_xO_2$ (b) with x = 0.0005, 0.005, 0.0,5 against Li in coin cells in function of the cycle number (zoom in inset, capacity retention on the right vertical axis), of the corresponding charge/discharge profiles of a representative cell in the 51st cycle (c) and (d) and of the corresponding differential capacity plots in the 51st cycle (e)–(f). The first two cycles were conducted at 0.1 C and the following 200 cycles at 1 C; the arrows are guides for the eyes.

Sum-up per element.—The previous discussion parts allowed to characterize and differentiate the impacts of the presence of Al, Fe and Li in the coprecipitation reaction, which are summarized in Table VII: aluminium was destabilizing the morphology and structure of the hydroxide very quickly, whereas iron did disturb the oxide structure and the lithium subtly templated the hydroxide and oxide structure. The electrochemical experiments revealed some negative influences of Al and Fe but above all highlighted the very low differences occurring at low impurity concentrations. One should therefore be careful regarding positive/negative effects in electrochemistry, being probably often more depending of the measuring devices and standards used[60,61] and of the cell quality than of the impurity itself.

Furthermore, interesting studies like the one of Touag et al.[62] on the one-pot coating of NMC 622 with Al in a coprecipitation reactor, showed that the presence of Al is not necessarily detrimental *per se*, but highly correlated to the timing of its introduction in the reaction. If Ni, Mn and Co have the time to coprecipitate freely at the start, their mixed hydroxide will not be disorganized by the following addition of aluminium sulfate. Of course, this should not happen in a practical recycling case, where Al would be present from the beginning of the coprecipitation but this highlights the complexity of the aluminium role.

As also concluded by Kim et al.[14] the effects of each impurity can be very different depending on various factors like the precursor nature and valence of the impurity or the way the study is conducted.

Table VII. Summary of the impurities influence on NMC 622 obtained by a classical coprecipitation method, depending of four main criteria and the tolerance threshold. The '/' symbol represents a neutral effect, whereas the minus sign stands for a negative effect.

Impurity	Morphology (hydroxide)	Structure	Specific capacity	Capacity retention	Tolerance threshold (x)
Al	—	Hydroxide (−) Oxide (/)	—	/	**0.0005**
Fe	/	Hydroxide (/) Oxide (−)	—	—	**0.005**
Li		/			**0.05**

It would then be very important in coming studies to choose and explain the synthesis set-up and process with great care and to characterize in detail the subtlest effect of each newly introduced element. Only so will it be possible to properly disentangle each influence in (future) studies were all these ions are mixed[63,64] and to satisfyingly compare different pieces of the scientific literature on resynthesis.

Conclusions

The goal of this work was to focus on the impact of three different elements, Al, Fe and Li, on the synthesis of a standard cathode active material, i.e. NMC 622. The first step was therefore to synthesize a reference material as pure as possible, with classical and scalable methods and with relevant particle morphology and discharge capacity values. This was accomplished by the use and fine tuning of a coprecipitation set-up and reaction, allowing to form quite spherical tertiary particles with a d_{50} diameter of 10 μm, the expected layered crystal structure and a specific capacity of around 150 mAh g^{-1} at 1 C. The remaining presence of very small amounts of a crystalline impurity and of diverse elements (Si, S, B, Zr, Al and Na) was reported. Based on this reference, the exact same process was applied in the presence of aluminium, iron or lithium sulfate with increasing concentration. Various effects were identified, depending on the introduced impurity: aluminium was found to rapidly alter the hydroxide morphology and crystal structure, iron to rather modify the oxide crystal structure and lithium to gently template the hydroxide and oxide structure, while being washed away and not being incorporated in the synthesized material. Based on these changes and their following impact on the electrochemical performances, different tolerance thresholds which should not be overcrossed were determined, to avoid any issue during resynthesis: $x_{Al} = 0.0005$ and $x_{Fe} = 0.005$. The presence of up to 1.0 at% of lithium was not detrimental throughout the CAM synthesis process and should not be a major issue for industrial application, as long as the coprecipitated product is washed thoroughly. This work was nonetheless perfectible and will be further developed by extending and refining the characterization of these Al, Fe and Li based materials. In-situ XRD analysis of the calcination step, as well as Mößbauer experiments on the iron-containing species are planned to get a deeper understanding of the crystal structure modifications induced by Al and Fe. The scale-up of the synthesis method established here is envisioned to reach the kg level in order to have enough material to produce industrially relevant electrode coatings and pouch cells. This should allow to compare the impurities influence with the lab-scale results and to reveal possible new effects in bigger cells and during long time cycling. At last, the mixing of these three elements in the coprecipitation synthesis should be conducted to look for cross-effects, as well as the use of a real resynthesis method with recyclate material to go beyond isolated impurities.

Acknowledgments

The authors are indebted to Dr V. Mereacre for the implementation and upkeep of the coprecipitation reactor, the gas stock, the cell parts and the gloveboxes, to M. Offerman and all the technical personal of IAM-ESS for various small measurements, everyday care of the laboratories and of the consumables and to T. Kaiser and P. Khelashvili of IAM-AWP for the ICP-OES measurements. This work contributes to CELEST (Center for Electrochemical Energy Storage Ulm-Karlsruhe) and was supported under the funding of the German Federal Ministry for Economic Affairs and Climate Action (BMWK) - Project LiBinfinity, FKZ: 16BZF339G.

ORCID

Johann Chable https://orcid.org/0000-0003-1134-766X
Nicole Bohn https://orcid.org/0009-0009-2753-3070
Shadi Al-Tobul https://orcid.org/0009-0001-2723-905X
Thomas Bergfeldt https://orcid.org/0000-0003-4595-7968
Marcus Müller https://orcid.org/0000-0002-5562-7201
Joachim R. Binder https://orcid.org/0000-0003-2237-1411

References

1. G. Losfeld, R. Mathieu, L. L'Huillier, B. Fogliani, T. Jaffré, and C. Grison, *Environ. Sci. Pollut. Res.*, **22**, 5608 (2015).
2. A. Beaudet, F. Larouche, K. Amouzegar, P. Bouchard, and K. Zaghib, *Sustain.*, **12**, 5837 (2020), https://mdpi.com/2071-1050/12/14/5837.
3. R. Yokoi, R. Kataoka, T. Maese, V. Bach, M. Finkbeiner, M. Weil, M. Baumann, and M. Motoshita, *Resour. Conserv. Recycl.*, **204**, 107526 (2024), https://linkinghub.elsevier.com/retrieve/pii/S0921344924001216.
4. M. Chen et al., *Sci. Rep.*, **9**, 1654 (2019), https://nature.com/articles/s41598-018-38238-3.
5. G. Azimi and K. H. Chan, *Resour. Conserv. Recycl.*, **209**, 107825 (2024), https://linkinghub.elsevier.com/retrieve/pii/S092134492400418X.
6. J. Amici et al., *Adv. Energy Mater.*, **12**, 2102785 (2022).
7. S. Jo et al., *Adv. Mater.*, **35**, 2207076 (2023).
8. H. Li, L. Wang, Y. Song, Z. Zhang, A. Du, Y. Tang, J. Wang, and X. He, *Adv. Mater.*, **36**, 2312292 (2024).
9. N. Zhang, Z. Xu, W. Deng, and X. Wang, *Electrochem. Energy Rev.*, **5**, 1 (2022).
10. H. Qiu et al., *Sustain*, **16**, 3876 (2024), https://mdpi.com/2071-1050/16/9/3876/htm.
11. N. Hayagan, I. Gaalich, P. Loubet, L. Croguennec, C. Aymonier, G. Philippot, and J. Olchowka, *Batter. Supercaps*, **7**, e202400120 (2024).
12. O. Celep, E. Y. Yazici, H. Deveci, and C. Dorfling, *Pamukkale Univ. J. Eng. Sci.*, **29**, 384 (2023), http://pajes.pau.edu.tr/eng/jvi.asp?pdir=pajes&plng=eng&un=PAJES-98793.
13. K. Binnemans and P. T. Jones, *J. Sustain. Metall.*, **9**, 1 (2023).
14. D. Kim et al., *J. Energy Chem.*, **95**, 446 (2024), https://linkinghub.elsevier.com/retrieve/pii/S2095495624002651.
15. M. Zybert, H. Ronduda, K. Dąbrowska, A. Ostrowski, K. Sobczak, D. Moszyński, B. Hamankiewicz, Z. Rogulski, W. Raróg-Pilecka, and W. Wieczorek, *Energy Reports*, **8**, 3995 (2022), https://linkinghub.elsevier.com/retrieve/pii/S2352484722005844.
16. C. Roitzheim et al., *ACS Appl. Energy Mater.*, **5**, 524 (2022).
17. S. Gao, X. Zhan, and Y. T. Cheng, *J. Power Sources*, **410–411**, 45 (2019), https://linkinghub.elsevier.com/retrieve/pii/S0378775318312023.
18. M. Eilers-Rethwisch, M. Winter, and F. M. Schappacher, *J. Power Sources*, **387**, 101 (2018), https://linkinghub.elsevier.com/retrieve/pii/S0378775318301988.
19. Z. Huang, Z. Wang, Q. Jin, H. Guo, X. Li, and Z. Yang, *Electrochim. Acta*, **192**, 120 (2016), https://linkinghub.elsevier.com/retrieve/pii/S0013468616301414.
20. Z. Y. Li, H. Guo, X. Ma, K. Sun, D. Chen, L. He, and S. Han, *J. Phys. Chem. C*, **123**, 19298 (2019).
21. O. A. Nasser and M. Petranikova, *Batter*, **7**, 60 (2021), https://mdpi.com/2313-0105/7/3/60/htm.
22. J. P. Peris Sastre, U. Saleem, E. Prasetyo, and S. Bandyopadhyay, *J. Clean. Prod.*, **429**, 139343 (2023), https://linkinghub.elsevier.com/retrieve/pii/S0959652623035011.
23. S. Kim, S. Park, M. Jo, M. Bak, J. Park, G. Jeong, J.-S. Yu, and K. Kwon, *J. Alloys Compd.*, **857**, 157581 (2021), https://linkinghub.elsevier.com/retrieve/pii/S0925838820339451.
24. R. Zhang et al., *ACS Sustain. Chem. Eng.*, **8**, 9875 (2020).

25. S. Park, D. Kim, H. Ku, M. Jo, S. Kim, J. Song, J. Yu, and K. Kwon, *Electrochim. Acta*, **296**, 814 (2019).
26. R. Zhang et al., *ACS Appl. Energy Mater.*, **4**, 10356 (2021).
27. M. Jo, H. Ku, S. Park, J. Song, and K. Kwon, *J. Phys. Chem. Solids*, **118**, 47 (2018).
28. S. Park, C. Jo, H. J. Kim, S. Kim, S.-T. Myung, H.-K. Kang, H. Kim, J. Song, J. Yu, and K. Kwon, *J. Alloys Compd.*, **835**, 155342 (2020), https://sciencedirect.com/science/article/pii/S0925838820317059.
29. J. Rodríguez-Carvajal, *Phys. B Condens. Matter*, **192**, 55 (1993), https://linkinghub.elsevier.com/retrieve/pii/0921452693901081.
30. A. L. Bail, H. Duroy, and J. L. Fourquet, *Mater. Res. Bull.*, **23**, 447 (1988), https://linkinghub.elsevier.com/retrieve/pii/0025540888900190.
31. A. Smith, P. Stüble, L. Leuthner, A. Hofmann, F. Jeschull, and L. Mereacre, *Batter. Supercaps*, **6**, e202300080 (2023).
32. M. Malik, K. H. Chan, and G. Azimi, *Mater. Today Energy*, **28**, 101066 (2022), https://linkinghub.elsevier.com/retrieve/pii/S2468606922001241.
33. A. Van Bommel and J. R. Dahn, *Chem. Mater.*, **21**, 1500 (2009).
34. R. B. Berk, T. Beierling, L. Metzger, and H. A. Gasteiger, *J. Electrochem. Soc.*, **170**, 110513 (2023).
35. Z. Meng, X. Ma, L. Azhari, J. Hou, and Y. Wang, *Commun. Mater*, **4**, 90 (2023), https://nature.com/articles/s43246-023-00418-8.
36. A. van Bommel and J. R. Dahn, *J. Electrochem. Soc.*, **156**, A362 (2009).
37. W. Hua et al., *J. Mater. Chem. A*, **5**, 25391 (2017).
38. S. Bette, B. Hinrichsen, D. Pfister, and R. Dinnebier, *J. Appl. Crystallogr.*, **53**, 76 (2020), https://journals.iucr.org/paper?po5156.
39. I. Rodrigues, J. Wontcheu, and D. D. MacNeil, *Mater. Res. Bull.*, **46**, 1878 (2011), https://linkinghub.elsevier.com/retrieve/pii/S002554081100359X.
40. W. Hua et al., *Chem. Mater.*, **32**, 4984 (2020).
41. R. B. Berk, T. Beierling, L. Metzger, and H. A. Gasteiger, *J. Electrochem. Soc.*, **170**, 110530 (2023), https://iopscience.iop.org/article/10.1149/1945-7111/ad0b42.
42. Q. Zhu, H. Xiao, R. Zhang, S. Geng, and Q. Huang, *Electrochim. Acta*, **318**, 1 (2019), https://linkinghub.elsevier.com/retrieve/pii/S001346861931134X.
43. X. Sun, J. Kim, and W. S. Kim, *Chem. Eng. J.*, **421**, 129924 (2021).
44. R. Ruess, M. A. Ulherr, E. Trevisanello, S. Schröder, A. Henss, and J. Janek, *J. Electrochem. Soc.*, **169**, 070531 (2022).
45. H. Park et al., *Nat. Chem.*, **14**, 614 (2022), https://nature.com/articles/s41557-022-00915-2.
46. B. Ying et al., *Chem. Mater.*, **35**, 1514 (2023).
47. J. Zhu and G. Chen, *J. Mater. Chem. A*, **7**, 5463 (2019), http://xlink.rsc.org/?DOI=C8TA10329A.
48. F. Wu, J. Tian, Y. Su, J. Wang, C. Zhang, L. Bao, T. He, J. Li, and S. Chen, *ACS Appl. Mater. Interfaces*, **7**, 7702 (2015).
49. X. Luo, X. Wang, L. Liao, S. Gamboa, and P. J. Sebastian, *J. Power Sources*, **158**, 654 (2006), https://linkinghub.elsevier.com/retrieve/pii/S0378775305013807.
50. H. Meng, P. Zhou, Z. Zhang, Z. Tao, and J. Chen, *Ceram. Int.*, **43**, 3885 (2017), https://linkinghub.elsevier.com/retrieve/pii/S0272884216323045.
51. M. Liang, D. Song, H. Zhang, X. Shi, Q. Wang, and L. Zhang, *ACS Appl. Mater. Interfaces*, **9**, 38567 (2017).
52. Y. Kim and D. Kim, *ACS Appl. Mater. Interfaces*, **4**, 586 (2012).
53. L. Bindi, A. G. Christy, S. J. Mills, M. E. Ciriotti, and E. Bittarello, *Can. Mineral.*, **53**, 791 (2015).
54. X. Zhao, F. Zhou, and J. R. Dahn, *J. Electrochem. Soc.*, **155**, A642 (2008).
55. A. Liu, N. Zhang, J. Li, T. Casagrande, C. Butcher, J. Martinez, A. Korinek, G. Botton, and J. R. Dahn, *J. Electrochem. Soc.*, **165**, A2781 (2018).
56. H. Ronduda, M. Zybert, A. Szczęsna-Chrzan, T. Trzeciak, A. Ostrowski, D. Szymański, W. Wieczorek, W. Raróg-Pilecka, and M. Marcinek, *Nanomaterials*, **10**, 2018 (2020), https://mdpi.com/2079-4991/10/10/2018.
57. H. Liang, S. Yuan, L. Shi, Y. Zhao, Z. Wang, and J. Zhu, *Chem. Eng. J.*, **394**, 124846 (2020), https://sciencedirect.com/science/article/pii/S1385894720308378?via%3Dihub.
58. Z. Yu, X. Qu, T. Wan, A. Dou, Y. Zhou, X. Peng, M. Su, Y. Liu, and D. Chu, *ACS Appl. Mater. Interfaces*, **12**, 40393 (2020).
59. R. Wang et al., *Nano Energy*, **62**, 709 (2019), https://sciencedirect.com/science/article/pii/S2211285519304951?pes=vor&utm_source=acs&getft_integrator=acs#sec5.
60. P. Stüble et al., *Batteries Supercaps*, **7**, e202400406 (2024).
61. R. Nölle, K. Beltrop, F. Holtstiege, J. Kasnatscheew, T. Placke, and M. Winter, *Mater. Today*, **32**, 131 (2020), https://linkinghub.elsevier.com/retrieve/pii/S1369702119307230.
62. O. Touag, G. Coquil, M. Charbonneau, G. Foran, A. Ghosh, D. Mankovsky, and M. Dollé, *Energy Adv.*, **2**, 701 (2023), https://pubs.rsc.org/en/content/articlehtml/2023/ya/d3ya00061c.
63. S. Krüger, C. Hanisch, A. Kwade, M. Winter, and S. Nowak, *J. Electroanal. Chem.*, **726**, 91 (2014), https://sciencedirect.com/science/article/pii/S1572665714002033?via%3Dihub.
64. M. Beak, J. Park, S. Park, S. Jeong, J. Kang, W. Choi, W-S. Yoon, and K. Kwon, *J. Hazard. Mater.*, **425**, 127907 (2022), https://sciencedirect.com/science/article/pii/S0304389421028764?via%3Dihub.